Central European Journal of Energetic Materials
ISSN 1733-7178; e-ISSN 2353-1843

Cent. Eur. J. Energ. Mater. 2023, *20*(2): 159-199; DOI 10.22211/cejem/168511
Article is available in PDF-format, in colour, at:
https://ipo.lukasiewicz.gov.pl/wydawnictwa/cejem-woluminy/vol-20-nr-2/

Research paper

Finite Volume Method for the Combustion Reaction of Energetic Materials

Yanchun Yu[1,*)], **Qiang Fu**[1,**)], **Jingxin Ma**[2)], **Weidong Chen**[2)], **Han Yan**[2)]

[1)] *School of Water Conservancy and Civil Engineering, Northeast Agricultural University, Harbin, 150030, China*

[2)] *School of Astronautics and Architectural Engineering, Harbin Engineering University, Harbin, 150001, China*

E-mails: *) yuyanchun@hrbeu.edu.cn; **) fuqiang@neau.edu.cn

Abstract: In order to analyse the effects of launch on the internal structure due to launch and given the relative paucity of experimental tests in this regime numerical simulations are an important method of prediction. Viscoelastic statistical crack mechanics offer a solution to the dynamic damage problems of explosives involved in explosion, impact and collision. Most finite element software does not include a viscoelastic statistical crack constitutive model; the model can only be embedded in the finite element software. Therefore, a computer program based on the finite volume method combined with viscoelastic statistical crack mechanics is presented, aiming to analyze the explosion problems more precisely and conveniently. A combustion equation of state is proposed to study the combustion reaction of explosives; the trends of temperature and stress of explosive during the combustion process are studied; Hot spot zones formed inside explosives are analyzed. The results are in accordance with the reaction law of combustion. The results indicate that when the bottom of the explosive charge is heated to a certain temperature, the explosive charge have a combustion reaction occurs. This conclusion has important value for studying the effect of the base gap on the launch safety of explosive munitions.

Keywords: finite volume method, viscoelastic statistical crack mechanics, combustion reaction, energetic materials, combustion equation of state

Abbreviations

EOS	Equation of state
FEM	Finite Element Method
FVM	Finite Volume Method
Visco-SCRAM	Viscoelastic Statistical Crack Mechanics

1 Introduction

The detonation of explosives is a very complicated process. As there is a paucity of experimental tests, numerical simulations are important for analyzing the detonations of explosives [1-5].The dynamic responses of explosives subjected to non-impact loads are very complex. A wide-pulse, low-amplitude load can be classified as a non-impact load, and its strength is relatively weak. Owing to the high risks from energetic materials, there are three main types of theoretical methods for analyzing the safety of energetic materials: macroscopic phenomenology, microscopic analysis, and macroscopic and microscopic combinations. The macroscopic phenomenology method is most widely used to study strong impact initiations [6-10]. The method can phenomenally describe the process of impact ignition; however, it does not describe the hot spot formation mechanism, and is not applicable to non-impact loads with low velocity and low pressure. The microscopic analysis method regards a macroscopic system as a set of several microscopic systems, and analyzes them as a whole. This method needs to be further explored and developed using theoretical methods and computing techniques. The macroscopic and microscopic combination method combines the macroscopic analysis and microscopic hot spot model, and performs an equivalent analysis based on a statistical method. A representative model using this method is the statistical crack mechanics (SCRAM) model proposed by Dienes and Kershner [11]. SCRAM is a representative constitutive model for studying the damage from energetic materials. Dienes *et al.* [12] performed many experiments on polymer-bonded explosives (PBXs), and gradually improved the SCRAM model. Addessio and Johnson [13] established an isotropic statistical crack mechanics model based on the SCRAM model; more specifically, they established an isotropic statistical mesoscopic damage constitutive model. Based on SCRAM and iso-SCRAM models, Bennett and Butler [14] established a thermo-force coupling model denoted “Viscoelastic Statistical Crack Mechanics” (Visco-SCRAM), which has mainly been used to study the non-impact ignition of the PBX9501 explosive [15-23]. Visco-SCRAM is a relatively complete constitutive model, and includes not only a microscopic

constitutive model for describing microcrack propagation, but also ignition and combustion models with chemical reactions.

The SCRAM model has been constantly developed and improved. Foreign researchers have embedded the model into finite element software packages such as DYNA3D, MESA, HYDROX, PRONTO, and ABAQUS to simulate typical problems such as impacts or impact detonations [11-12, 24]. Sun [25] embedded the Visco-SCRAM model into LS-DYNA software, the mechanical response, damage response and temperature rise response of PBX explosive in the process of three-way compression, motion in the chamber and penetration are studied. Zhang *et al.* [26] improved the Visco-SCRAM model, and embedded the improved model into the finite element software to simulate a plate impact experiment for a PBX. Therefore, most research has been based on embedding the Visco-SCRAM model into the finite element software for dynamic response analyses of explosives, and has only considered a single stage of explosive reaction, such as ignition, combustion, or detonation. No numerical method has been established for analyzing the entire reaction process of explosives based on the Visco-SCRAM model.

Finite volume method (FVM) is widely used in the field of computational fluid dynamics [27-32]. Compared with the finite element method (FEM) [33, 34], the FVM has clear physical significance, a simple and discrete process, easy programming, and is suitable for solving complex boundary problems. Moreover, an FVM using an explicit integral algorithm is more suitable for solving highly nonlinear problems such as explosions, impacts, and collisions. At present, few studies have applied the FVM to solve nonlinear dynamics problems such as explosions and impacts. Therefore, an FVM combined with the Visco-SCRAM model is proposed in this study, aiming to establish a relatively complete numerical method for analyzing the dynamic responses of energetic materials subjected to a wide-pulse and low-amplitude load. This research provides certain innovations, as discussed below.

2 FVM

2.1 Discretization equation of FVM

The basic assumptions of continuum mechanics indicate that the continuum should satisfy the conservations of mass, momentum, and energy. The FVM is a conservative governing equation. FVM automatically satisfies the mass conservation equation. In addition, the momentum conservation equation is discretized, and the energy conservation equation is updated.

The FVM, like the finite element method, discretizes the solution domain and divides it into grids. The key step of the FVM comprises integrating the differential equation in the control volume and deducing its discrete equation. The physical meaning of this discrete equation is the flux balance of the control volume, and each term of the equations has a definite physical meaning.

A two-dimensional unstructured grid is shown in Figure 1. The solid line divides the solution domain into a triangular mesh. The control volume is formed by connecting the center of gravity and midpoints of each side of the triangular mesh. The closed polygon enclosed by the dashed line is the control volume and *P* is the center of the control volume.

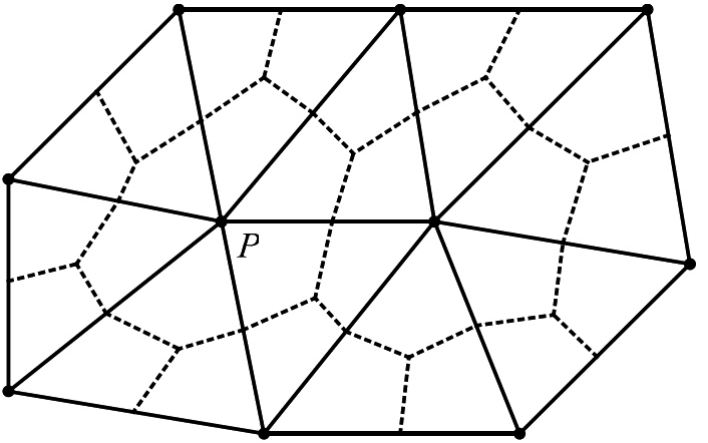

Figure 1. Control volume

The expression for integrating the momentum conservation equation into the control volume is as follows:

$$\int_V \rho \ddot{u}_i dV = \int_V \left(\rho b_i + \frac{\partial \sigma_{ij}}{\partial x_j} \right) dV \tag{1}$$

where $\ddot{u}_i$ ($i = 1, 2, 3$) denotes the displacement component of the control volume, and $\ddot{u}_i$ is a constant in the control volume. When all the control volumes satisfy Equation 1, then momentum is conserved throughout the domain. If the body force is ignored and the volume integral is converted into a surface integral by Gaussian integration, Equation 1 can be rewritten as follows:

$$\int_V \rho \ddot{u}_i dV = \int_S \sigma_{ij} n_j dS \tag{2}$$

where n_j (j = 1, 2, 3) denotes the component of the outward normal vector (n) of the control volume surface (S). To calculate the integral on the right side of Equation 2, it is necessary to assume the distribution of stress in the grid. For the two-dimensional grid shown in Figure 1, we assume that the stresses in the triangular mesh are constant, and that the stress on the boundary of the control volume is also constant. Thus, the right side of Equation 2 is as follows:

$$\int_S \rho \ddot{u}_i dS = \int_L \sigma_{ij} n_j dl = \int_L \sigma_{i1} dy - \sigma_{i2} dx \quad (i = 1, 2) \tag{3}$$

where n_j (j = 1, 2) denotes the outward normal vector of curve (L), and L is the boundary of the control volume. Finally, the two-dimensional equilibrium equations for the control volume are as follows:

$$\int_S \rho \ddot{u}_x dxdy = \int_L \sigma_{xx} dy - \sigma_{xy} dx \tag{4}$$

$$\int_S \rho \ddot{u}_y dxdy = \int_L \sigma_{xy} dy - \sigma_{yy} dx \tag{5}$$

where $\ddot{u}_x$ and $\ddot{u}_y$ denote the components of acceleration in each direction, and ρ denotes the density of the control volume.

For the two-dimensional grid shown in Figure 1, if the control volume centered on P is connected with m triangular meshes, the left side of Equation 2 is as follows:

$$\int_V \rho \ddot{u}_i dV = \int_S \rho \ddot{u}_i dS = \frac{\ddot{u}_i \rho}{3} \sum_{n=1}^{m} S_n = M_p \tag{6}$$

where S_n is the area of each triangular grid connected to the center P of the control volume.

The detailed discrete process of the FVM is provided in extant studies [35]. The final discrete equations are as follows:

$$M_p \ddot{u}_{xp} = \sum_{n=1}^{n_{p3}} (\sigma_{xx})_n (a_p)_n - \sum_{n=1}^{n_{p3}} (\sigma_{xy})_n (b_p)_n + \int_L \overline{X} dl \tag{7}$$

$$M_p \ddot{u}_{yp} = \sum_{n=1}^{n_{p3}} \left(\sigma_{xy}\right)_n \left(a_p\right)_n - \sum_{n=1}^{n_{p3}} \left(\sigma_{yy}\right)_n \left(b_p\right)_n + \int_p \bar{Y} dl \tag{8}$$

where M_p denotes the mass of the control volume centered on node P, and $\ddot{u}_{xp}$ and $\ddot{u}_{yp}$ denote the acceleration components of node P in the x and y directions, respectively. Furthermore, n_{p3} denotes the total number of triangular elements associated with node P. Additionally, $\bar{X}$ and $\bar{Y}$ denote the densities of the external forces on the surface in the x and y directions, respectively, and $(a_p)_n$ and $(b_p)_n$ are coefficients of the control volume centered on node P.

2.2 Solving FVM

The discrete equation obtained above is coupled with the constitutive equation, state equation, *etc.*, and the quantities of each state are connected. The detailed calculation process is shown in Figure 2.

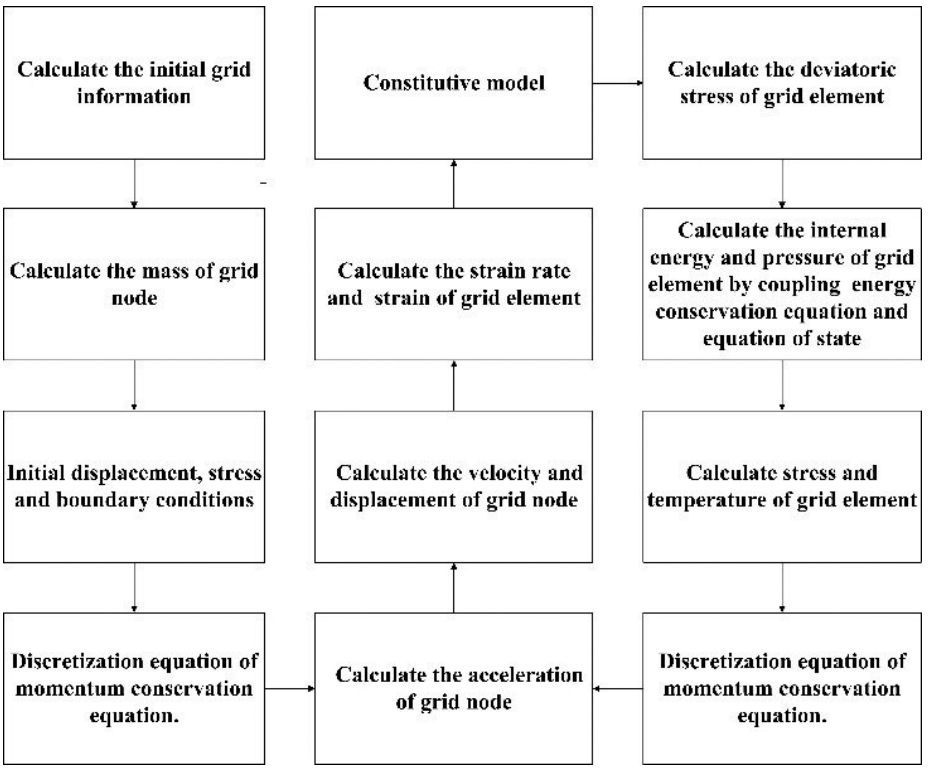

Figure 2. Calculation flow chart

2.3 Comparative verification of FVM and FEM

To verify the accuracy of the FVM proposed in this study, the calculation results of the FVM and FEM are compared and analyzed based on an example. Taking a two-dimensional thin steel plate as an example, the calculation model of the thin steel plate is 1×0.02 m, and the two ends of the steel plate are fixed ends, as shown in Figure 3. The mesh is divided along the length and thickness of the steel plate. They are divided into 500 along the length direction and 10 along the thickness direction, which are divided into triangular elements. The plate surface is subjected to a uniformly distributed load as shown in Equation 9.

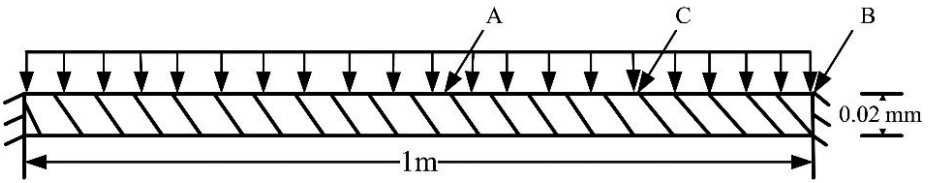

Figure 3. Calculation model for thin steel plate

$$P(t)=\begin{cases}-0.5\ \text{MPa/m} & t\le 1\text{s}\\ 0 & t>1\text{s}\end{cases} \tag{9}$$

The constitutive model of the steel plate is an elastic-plastic strength model. The material parameters of the constitutive model are as follows:

- the density is 7830 $kg\cdot m^{-3}$,
- elasticity modulus is 2.07×10^{11} Pa,
- tangent modulus is 5.0×10^{9} Pa,
- yield stress is 4.0×10^{8} Pa, and
- Poisson's ratio is 0.3.

The values of the material parameters are obtained from the material library of AUTODYN. The transient dynamic response of the plate is calculated.

The finite element method has been widely accepted for solving the transient dynamic response problems of steel plates subjected to pressure loads, and the calculation accuracy is high. Therefore, it is feasible to compare the calculation results of the FVM and finite element method in this study.

The FVM and LS-DYNA are used to calculate the transient dynamic response of the steel plate subjected to a pressure load. The results of the two methods are compared, and the time-history curves of the displacement and stress of the model at points A, B and C are shown in Figures 4 and 5.

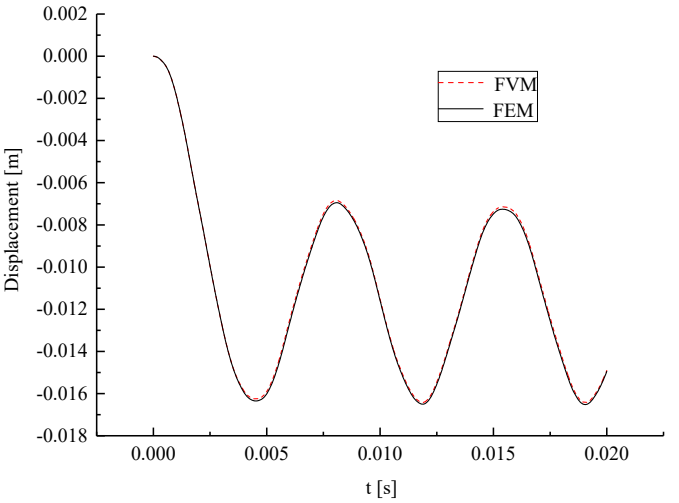

(a)

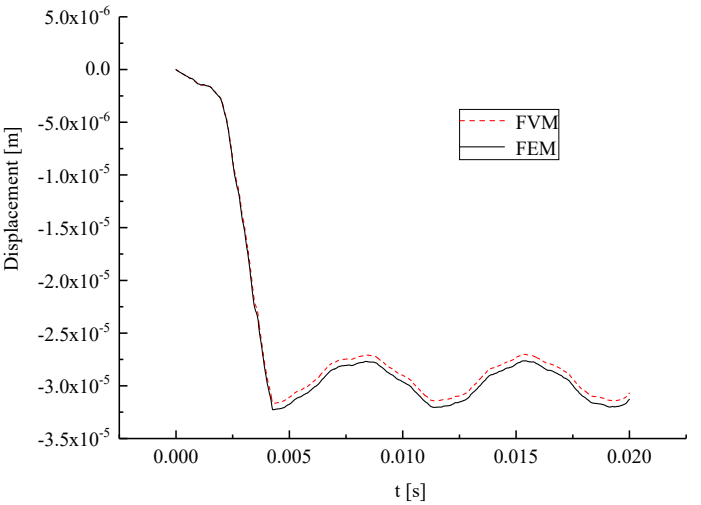

(b)

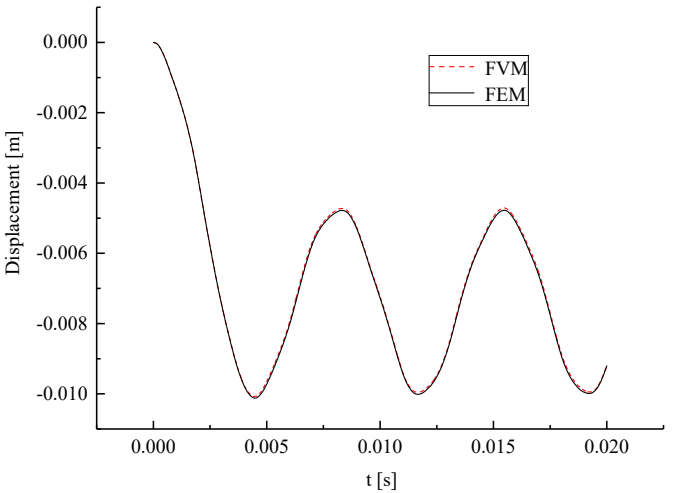

(c)

Figure 4. Comparison diagram of displacement between FEM and FVM at points: A (a), B (b) and C (c)

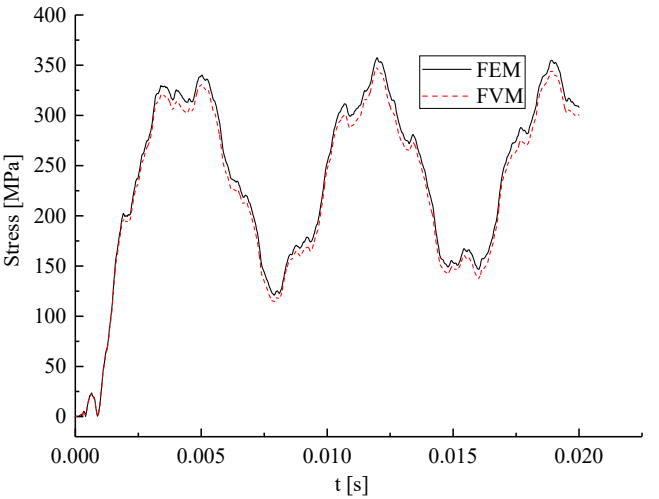

(a)

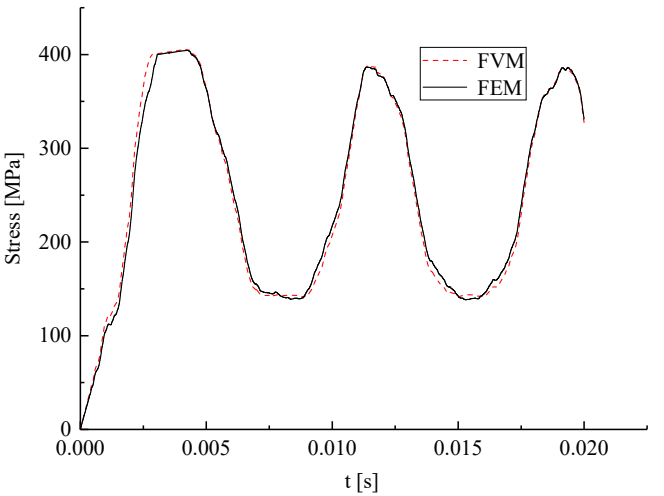

(b)

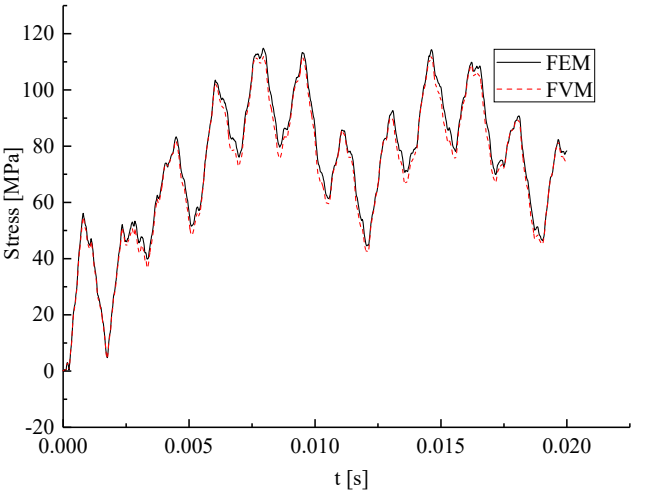

(c)

Figure 5. Comparison diagram of stress between FEM and FVM at points: A (a), B (b) and C (c)

The results show that the results of the FVM are basically consistent with those of the finite element method. The utility of the FVM is therefore demonstrated in the relatively simple scenario. Near the extreme value of the stress, the results of FVM show a small numerical oscillation; On the one hand, due to the difference between the explicit algorithm and the implicit algorithm,

the total number of calculation steps of the explicit algorithm is much more than that of the implicit algorithm, so it shows more details than the implicit algorithm; On the other hand, the stress propagates in the structure in the form of waves, when the structure is subjected to similar impact loads, the physical quantities such as stress will also change suddenly, which may cause the discontinuity of the physical quantities on both sides of the wave front, thus the solution of differential equations brings instability.

3 Visco-SCRAM Model

Visco-SCRAM is a relatively complete constitutive model. It includes not only a microscopic constitutive model for describing microcrack propagation, but also ignition and combustion models with chemical reactions. The specific theory of this model is provided in extant studies [13, 36]. Therefore, only a summary is provided here.

A viscoelastic body consists of a series of viscous and elastic elements, The deviatoric stress of the viscous element is the same as that of the elastic element, and both are equal to the deviatoric stress of Maxwell body. The sum of the deviator strain of elastic element and viscous element is the deviator strain of viscoelastic body. In Maxwell's viscoelastic body model, the relation between deviator stress and deviator strain of elastic element is

$$S_{ij}^{e} = 2Ge_{ij}^{e}, \tag{10a}$$

the relation between deviator stress and deviator strain rate of viscous element is

$$S_{ij}^{v} = 2\eta\dot{e}_{ij}^{v}, \tag{10b}$$

the sum of the deviator strain rate of the elastic element and the deviator strain rate of the viscous element is the deviator strain rate of the viscoelastic body. Therefore, the relation between the deviator stress rate and the deviator strain rate of the viscoelastic body is as follows:

$$\dot{S}_{ij}^{ve} = 2G\dot{e}_{ij}^{ve} - \frac{S_{ij}^{ve}}{\tau} \tag{10c}$$

where τ is relaxation time ($\tau = \eta/G$), G is shear modulus of the elastic element, η is the viscosity coefficient of the viscous element, and $\dot{e}_{ij}^{ve}$ is the deviator strain rate of viscoelastic body.

The generalized viscoelastic body is generally composed of N viscoelastic elements. The generalized viscoelastic body has the same deviator strain rate as each viscoelastic body, and the generalized viscoelastic body has the sum of the deviator stresses of N viscoelastic elements, that is

$$S_{ij}^{ve} = \sum_{n=1}^{N} S_{ij}^{ve(n)} \tag{10d}$$

$$\tau = \sum_{n=1}^{N} \tau^{(n)} \tag{10e}$$

$$G = \sum_{n=1}^{N} G^{(n)} \tag{10f}$$

Then, the relation between deviator stress rate and deviator strain rate of generalized viscoelastic body is as follows:

$$\dot{S}_{ij} = \sum_{n=1}^{N} \left(2G^{(n)} \dot{e}_{ij}^{ve} - \frac{S_{ij}^{ve(n)}}{\tau^{(n)}} \right) \tag{11}$$

where, $G^{(n)}$ is the shear modulus of the n-th elastic element, $S_{ij}^{(n)}$ is the deviatoric stress of the n-th viscoelastic body, and the relation between the deviator stress rate and the deviator strain rate of the n-th viscoelastic element is as follows:

$$\dot{S}_{ij}^{ve(n)} = 2G^{(n)} \dot{e}_{ij}^{ve} - \frac{S_{ij}^{ve(n)}}{\tau^{(n)}} \tag{12}$$

In 1990, Addessio and Johnson obtained the relationship between deviated strain and deviated stress in a microcracked body,

$$e_y^c = \beta^e c^3 S_{ij} \tag{13}$$

where c is mean crack radius, β^e is a parameter related to shear modulus and initial crack distribution N_0,

$$2G\beta^e = AN_0 \equiv \frac{1}{a^3} \tag{14}$$

where, a is initial crack size, the relationship between partial strain and crack radius is as follows:

$$2Ge_{ij}^{c} = (\frac{c}{a})^{3} S_{ij} \tag{15}$$

And the relationship between the partial strain rate and the crack radius is as follows:

$$2G\dot{e}_{ij}^{c} = 3\left(\frac{c}{a}\right)^{2}\frac{\dot{c}}{a}S_{ij} + \left(\frac{c}{a}\right)^{3}\dot{S}_{ij} \tag{16}$$

where $\dot{c}$ is crack speed. Dienes described the evolution and growth of cracks; it is assumed that the crack growth rate is related to the stress intensity factor. The crack growth can be expressed as follows:

$$\begin{aligned} \dot{c} &= v\left(\frac{K}{K_1}\right)^{m}_{max} && K < K' \\ \dot{c} &= v\left(1 - \left(\frac{K_0}{K}\right)^{2}\right)_{max} && K \geq K' \end{aligned} \tag{17}$$

where m denotes a factor of the crack speed growth, v_{max} denotes the terminal crack speed, and K_0 denotes the fracture toughness. Furthermore, K denotes the stress intensity factor, and K_1 is a constant. The values of K' and K_1 are determined as follows:

$$\begin{aligned} K' &= K_0\sqrt{1+\left(\frac{2}{m}\right)} \\ K_1 &= K_0\sqrt{1+\left(\frac{2}{m}\right)}\left[1+\frac{m}{2}\right]^{\frac{1}{m}} \end{aligned} \tag{18}$$

The equivalent strength factor K of viscoelastic statistical crack model is as follows:

$$K^{2} = \pi \cdot c \cdot \sigma_{eff} = \frac{3}{2}\pi \cdot c \cdot S_{ij}S_{ij} \tag{19}$$

where σ_{eff} is equivalent stress:

$$\sigma_{eff} = \sqrt{\frac{3}{2} S_{ij} S_{ij}} \tag{19a}$$

In the generalized viscoelastic statistical crack model, the deviatoric stress of the generalized viscoelastic statistical crack model, the deviatoric stress of the generalized viscoelastic body and the deviatoric stress of the microcracked body are equal to S_{ij}. In the viscoelastic crack constitutive model, the partial strain rate is composed of the partial strain rate of the viscoelastic body and the partial strain rate of the microcracked body, which is as follows:

$$\dot{e}_{ij} = \dot{e}_{ij}^{ve} + \dot{e}_{ij}^{c} \tag{20}$$

According to Equations 11, 16 and 20, the deviatoric stress rate of generalized viscoelastic statistical crack model can be expressed as follows:

$$\dot{S}_{ij} = \frac{2G\dot{e}_{ij} - \sum_{n=1}^{N} \frac{S_{ij}^{(n)}}{\tau^{(n)}} - 3(\frac{c}{a})^2 \frac{\dot{c}}{a} S_{ij}}{1 + (\frac{c}{a})^3} \tag{21}$$

where S_{ij} denotes the deviatoric stress, G denotes the shear modulus of the elastic element, $S_{ij}^{(n)}$ denotes the deviatoric stress of the nth viscoelastic body, $\tau^{(n)}$ denotes the relaxation time of the nth viscoelastic body, c denotes the mean crack radius, $\dot{c}$ denotes the crack growth rate, and a denotes an initial parameter. The deviatoric stress rate of each viscoelastic element is as follows:

$$\dot{S}_{ij}^{(n)} = 2G^{(n)}\dot{e}_{ij} - \frac{S_{ij}^{(n)}}{\tau^{(n)}} - \frac{G^{(n)}}{G}\left[3\left(\frac{c}{a}\right)^2 \frac{\dot{c}}{a} S_{ij} + \left(\frac{c}{a}\right)^3 \dot{S}_{ij}\right] \tag{22}$$

where $G = \sum_{n=1}^{N} G^{(n)}$, $G^{(n)}$ denotes the shear modulus of the n-th elastic body.

4 Macroscopic Volume Heating Model of a Viscoelastic Statistical Cracked Body

The thermodynamic equation introduced in this study to calculate the temperature of energetic materials is from the macroscopic volume heating model. This model includes mechanical terms that describe the viscosity, crack damage, and adiabatic volume changes, along with a chemical thermal decomposition term. The chemical thermal decomposition is described by the Arrhenius first-order reaction kinetics model. During non-impact ignition, the time and space scales of heat conduction of macroscopic continuum in each unit of energetic material is relatively large, they are generally much larger than those of other heating mechanisms. Therefore, the heat conduction term can be ignored for the entire heat change during the non-impact ignition [37]. Therefore, the temperature variation equation with respect to time can be simplified as follows:

$$\dot{T} = -\gamma T \dot{\varepsilon}_{ii} + \frac{I}{\rho C_V}\left(\dot{W}_{ve} + \dot{W}_{cr}\right) + \frac{\Delta H}{C_V} Z \, exp\left(-\frac{E_A}{RT}\right) \tag{23}$$

where T denotes the temperature, γ denotes the Gruneisen coefficient, C_V denotes the constant-volume specific heat, $\dot{W}_{ve}$ denotes the vicious power, $\dot{W}_{cr}$ denotes the crack damage power, and ΔH, E_A, and Z denote the unit mass decomposition heat, activation energy, and preexponential factor of the thermal decomposition reaction of the energetic materials, respectively. The variables correspond to each other as follows:

$$\dot{W}_{ve} = \sum_{n=1}^{N} S_{ij}^{(n)} \dot{e}_{ij}^{ve} = \sum_{n=1}^{N} \frac{S_{ij}^{(n)} S_{ij}^{(n)}}{2G^{(n)} t^{(n)}} \tag{24}$$

$$\dot{W}_{cr} = S_{ij} \dot{e}_{ij}^{cr} = \frac{1}{2G}\left[3\left(\frac{c}{a}\right)^2 \frac{\dot{c}}{a} S_{ij} S_{ij} + \left(\frac{c}{a}\right)^3 \dot{S}_{ij} S_{ij}\right] \tag{25}$$

The temperature change of the viscoelastic statistical cracked materials in an element is described in Equation 23. All of the variables in the equation, with the exception of the temperature, can be solved for using the viscoelastic statistical crack model. Therefore, this equation can be regarded as an ordinary differential equation with respect to the temperature, and the temperature of an element can be obtained by integration with respect to time.

5 Analysis of Ignition Performance of Explosive

In this section, an example is used to study the ignition performance of explosives subjected to a low-amplitude and wide-pulse load. Based on the FVM, the ignition temperature and critical non-impact load of the explosive are studied using the Visco-SCRAM model and Jones-Wilkins-Lee (JWL) equation of state (EOS). The JWL EOS is as follows:

$$p = A(1-\frac{w}{R_1V})\mathrm{e}^{-R_1V} + B(1-\frac{w}{R_2V})\mathrm{e}^{-R_2V} + \frac{wE}{V} \tag{26}$$

where A, B, R_1, R_2, and w denote the material parameters, p denotes the pressure, E denotes the internal energy per unit initial volume, and V denotes the relative volume.

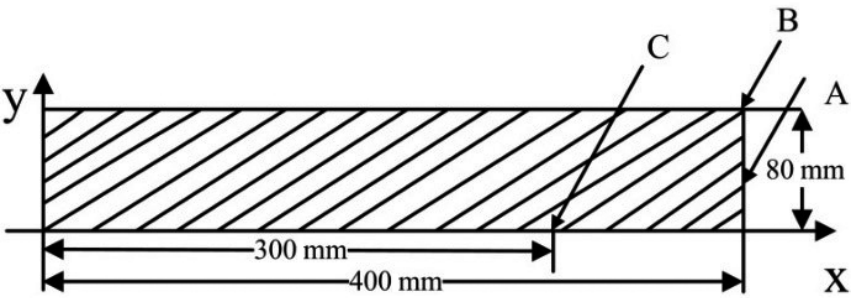

Figure 6. Calculation model

The explosive model is shown in Figure 6. The explosive model is an axisymmetric model, where the X-axis is the symmetry axis. The total length of the axis of symmetry is 40 cm, and the maximum radius of the model is 8 cm. The load is applied at the far-right side of the model (bottom of the explosive, x = 400 mm), the far-left side of the model is a free boundary, and the X-axis is a symmetric boundary condition (UY = 0). The explosive model is divided into 4574 triangular elements and 2408 nodes.

The PBX9501 explosive was used in this study. The relevant parameters of the PBX9501 explosive are provided in extant studies [38]. The viscoelastic parameters, statistical crack parameters, relaxation parameters, and thermodynamic parameters of the PBX9501 explosive are provided in Tables 1 to 5 [38].

Table 1. Viscoelasticity parameters ($G^{(1)}$ denotes the shear modulus of the 1st elastic element, $G^{(2)}$ denotes the shear modulus of the 2nd elastic element, and the series continues)

$G^{(1)}$ [Pa]	$G^{(2)}$ [Pa]	$G^{(3)}$ [Pa]	$G^{(4)}$ [Pa]	$G^{(5)}$ [Pa]
0.944×10^8	1.738×10^8	5.212×10^8	9.085×10^8	6.875×10^8

Table 2. Crack parameters of the explosive (v denotes the Poisson's ratio, m denotes the factor of the crack speed growth, c_0 denotes the mean initial crack radius, a denotes the initial model parameter, v_{max} denotes the terminal crack speed, and K_0 denotes the fracture toughness)

v	M	c_0 [m]	a [m]	v_{max} [m·s^{-1}]	K_0 [Pa·m$^{1/2}$]
0.3	10	0.00003	0.001	300	5×10^5

Table 3. Thermodynamic parameters of the explosive (k_i denotes the thermal conductivity, C_V denotes the heat capacity at constant volume, ρ denotes the density, ΔH denotes the heat of reaction per unit mass for chemical decomposition, Z denotes the preexponential factor, E_A denotes the activation energy, and R denotes the universal gas constant)

k_i [W·m^{-1}·K^{-1}]	C_V [J·kg^{-1}·K^{-1}]	ρ [kg·m^{-3}]	ΔH [J·kg^{-1}]	Z [m·s^{-1}]	E_A/R [K]
0.5	1200	1810	5.5×10^6	5×10^9	2.652×10^4

Table 4. Relaxation parameters (τ denotes the relaxation time)

$1/\tau^{(1)}$ [s]	$1/\tau^{(2)}$ [s]	$1/\tau^{(3)}$ [s]	$1/\tau^{(4)}$ [s]	$1/\tau^{(5)}$ [s]
0	7.32×10^3	7.32×10^4	7.32×10^5	2.00×10^6

Table 5. Material parameters of the EOS [39]

A [Mbar]	B [Mbar]	R_1	R_2	w
7.781×10^2	-5.031×10^{-2}	11.3	1.13	0.8938

The pressure load applied at the far-right side of the model (bottom of the explosive, x = 400 mm), and it is a sinusoidal load, as follows:

$$F(t) = 400 \times 10^6 \times \sin(2.0\pi/200 \times 10^{-6} \times t) \text{ [Pa·m}^{-1}\text{]} \ (0 \leq t \leq 100 \text{ μs}) \quad (27)$$

The initial temperature at the bottom of the explosive is set to 300 and, 400 K respectively, and the temperature of the other parts of the explosive model is set to 300 K. Based on the FVM, the time histories of the temperature and stress

of the explosive subjected to the load are calculated by the computer program developed in this study. The ignition performance of the explosive model is discussed. The results are shown in Figures 7 and 8.

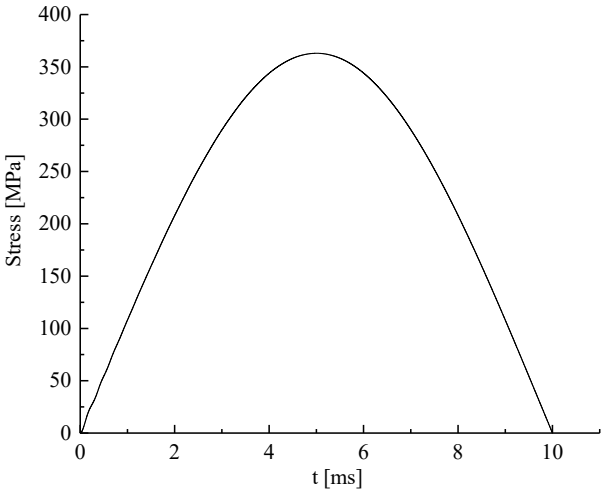

(a)

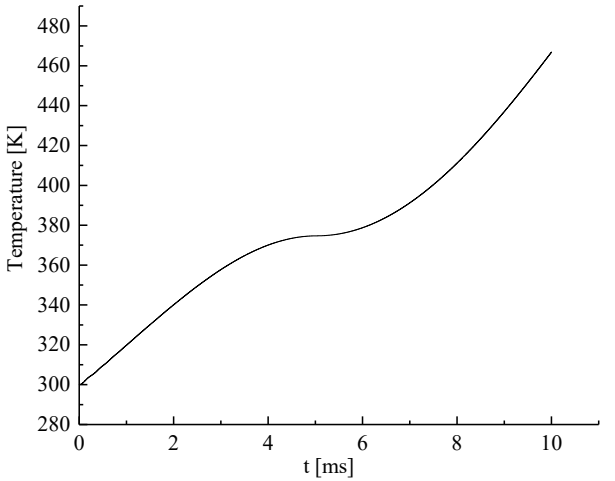

(b)

Figure 7. Time history curve of stress at bottom of explosive (a) and time history curve of temperature at bottom of explosive (b), both for the initial temperature at the bottom of the explosive of 300 K

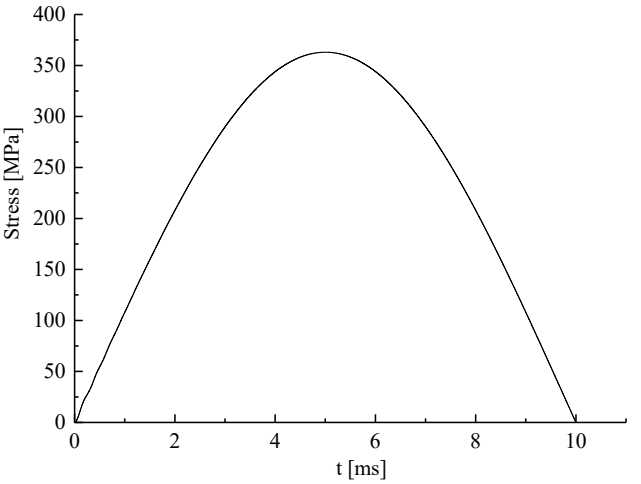

(a)

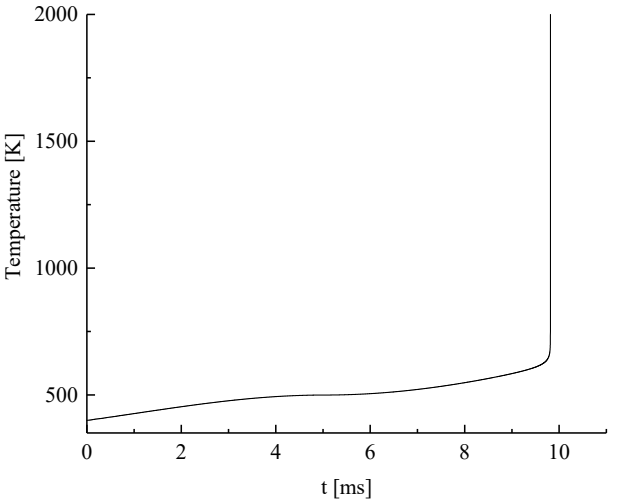

(b)

Figure 8. Time history curve of stress at bottom of explosive (a) and time history curve of temperature at bottom of explosive (b), both for the initial temperature at the bottom of the explosive of 400 K

It can be seen from Figure 7(a) that when the time is 5 ms, the maximum stress value of the explosive is approximately 350 MPa, and this maximum appears at the bottom of the explosive. Figure 7(b) shows that the highest

temperature at the bottom of explosive is about 540 K, it is far less than the ignition temperature of the explosive.

It can be seen from Figure 8(a) that when the time is 5 ms, the maximum stress value of the explosive is approximately 350 MPa, and this maximum appears at the bottom of the explosive. In Figure 8(b), when the calculation time is before 9 mm, the temperature of the explosive increases slowly, and the time history curve of the explosive tends to be stable. When the calculation time is close to 10 ms, the temperature suddenly increases sharply, and the value of the temperature increases infinitely. Based on the chemical kinetic Arrhenius equation used in this study, the ignition temperature criterion is $dT/dt \rightarrow \infty$ [39], indicating that the temperature at the bottom of the explosive has reached the ignition temperature, and thus the explosive is ignited. In addition, the temperature time-history curve in Figure 8 shows that when the temperature suddenly increases sharply, the temperature of the explosive is between 750 and 800 K, indicating that the ignition temperature of the explosive is between 750 and 800 K.

6 Validation of the Results

Relatively little research has been conducted on the ignition performances of explosives subjected to pressure loads based on Visco-SCRAM. No relevant test results have yet been verified. To prove the correctness of the method proposed in this study, the results in Figure 8(b) in this study are compared with those from existing research for verification [37].

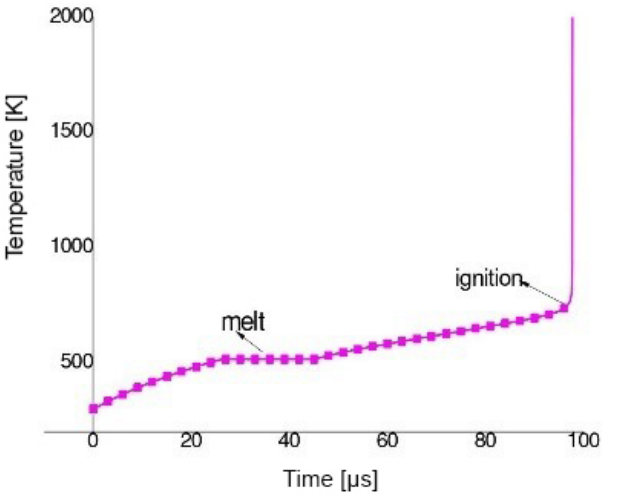

(a)

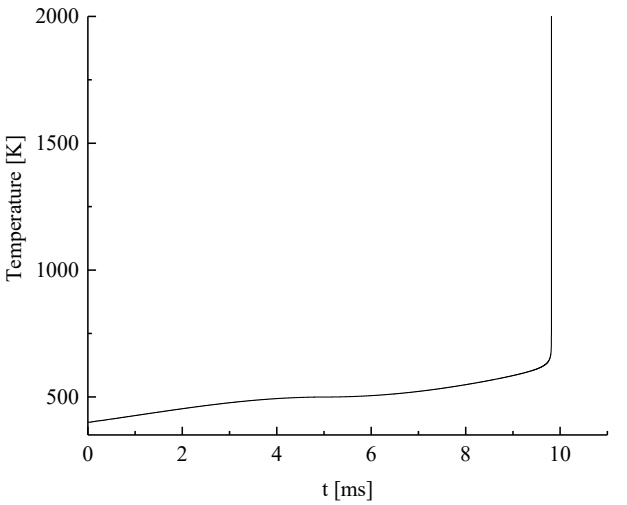

(b)

Figure 9. Comparison of temperature variation: results of the existing research [13] and results of this study in Figure 8(b) (b)

Zhao [37] calculated the thermal and mechanical responses of PBX-9501 samples using shear drilling tests. The finite element model of the shear drilling test is shown in Figure 4.7 in Zhao's study [37]. The length of the impact and input bars was 25 cm. The length of the output bar was 1.55 cm, and the diameter

of the bar was 1.27 cm. The fixator, impact bar, input bar, and output bar were divided by a Lagrange grid, and the explosive samples were divided by a pure Euler grid. A fluid-solid coupling algorithm was used to create the interactions between the two materials described by two types of grids. In the calculation model, the input bar, output bar, and sample clamps were 350-Magens steel, and were described by the elastic-plastic material model. The sample of the PBX-9501 explosive was described by the Visco-SCRAM model, and the constitutive model subroutine was embedded into LS-DYNA software to simulate the dynamic shear drilling test of the PBX-9501 explosive. When the impact bar hit the input bar at 26 $m \cdot s^{-1}$, the time-history variations of the internal pressure, strain rate, and temperature of the explosive were analyzed, and the ignition of the explosive subjected to the impact velocity was studied. The temperature time-history curve from Sihai's study is shown in Figure 9(a).

The temperature time-history curve from this study is shown in Figure 9(b). As the explosive model, loading mode, and loading intensity investigated in this study are different from the problems studied in the existing research, the variation laws of the temperature are different. However, the explosive both are PBX-9501, so the ignition performances of the explosives are the same. Therefore, it is feasible to compare the results of the two methods regarding the ignition performance of explosives.

The conclusion in the existing research [37] is that the ignition temperature of the explosive, *i.e.* approximately 784 K. In this study, the result is that the ignition temperature of the explosive is between 750 and 800 K. The results of the two methods are basically consistent. Therefore, the correctness of the method in this study was further verified.

7 Analysis of Combustion Reaction of Explosive

7.1 Mixed combustion EOS

The combustion reaction of the explosives is studied in this section. A reasonable EOS is the key to accurately describing the combustion reaction of explosives. A mixed combustion EOS is generally used to describe the combustion reaction of an explosive. The combustion reaction of the explosive is in a two-phase state. The temperature of the explosive is used as the criterion. When the temperature of the explosive is less than or equal to the melting temperature of the explosive, *i.e.* $T \leq T_{melt}$, it means that no chemical reaction has occurred in the explosive, and that the explosive is in the solid phase. The solid JWL EOS is adopted in this stage. When the temperature of the explosive is greater than or equal to the

ignition temperature of the explosive, *i.e.* $T \geq T_{ignition}$, it indicates that a chemical reaction has occurred in the explosive, and that the explosive is in the gas phase. The virial EOS is used in this stage. When the temperature of the explosive is between the melting temperature and ignition temperature, that is, $T_{melt} < T < T_{ignition}$, the explosive is in a two-phase state, and the EOS is a mixed EOS of the gas JWL and the virial EOS. The pressure calculation of the mixed state is based on the reaction degree of the explosive. The reaction degree of the explosive (F) is related to the temperature of the explosive. The reaction degree of the explosive is calculated as follows:

$$F = (T - T_{melt}) / (T_{ignition} - T_{melt}) \tag{28}$$

where T denotes the current temperature of the explosive, T_{melt} denotes the melting temperature of the explosive and $T_{ignition}$ denotes the ignition temperature of the explosive.

When the explosive is in a two-phase state, the JWL EOS is used to calculate the pressure of the current time step, denoted as P_1. Simultaneously, the virial EOS is also used to calculate the pressure of the current time step, denoted as P_2. Equation 28 is used to calculate the reaction degree of the current time step. The pressure of the current time step in the two-phase state is as follows:

$$P = P_1 + P_2 F \tag{29}$$

where P denotes the pressure of the current time step in the two-phase state, and F denotes the reaction degree of the explosive. The JWL EOS is given by Equation 26. The virial EOS can accurately establish the relationship between the parameters and intermolecular forces of the gases [40]. The virial EOS for 1 molar gas is as follows:

$$PV / RT = 1 + B(T) / V + C(T) / V^2 + D(T) / V^3 + ... \tag{30}$$

where V is the molar volume, P is the pressure, R is the universal gas constant, T is the temperature, and B, C, and D are parameters. The virial EOS for n molar gas is as follows:

$$PV / nRT = 1 + B(T) / V + nC(T) / V^2 + ... \tag{31}$$

where n denotes the amount of the substance. It can be seen that Equations 30 and 31 are related to the temperature-dependent quantities, such as $B(T)$,

$C(T)$, and $D(T)$. These quantities are defined as the second virial coefficient, the third virial coefficient, the fourth Virial coefficient, *etc.* According to statistical mechanics, the virial coefficient is expressed by a molecule potential function. The physical meaning of the virial EOS is clear. The first term on the left side of the equation corresponds to the ideal gas EOS, the second term on the right side of the equation describes the interaction between the two molecules, the third term on the right side of the equation considers the interactions between the three molecules, and so on. The detailed theory of the virial EOS can be found in extant studies [40]. The calculation process for the combustion reaction of the explosive is shown in Figure 10.

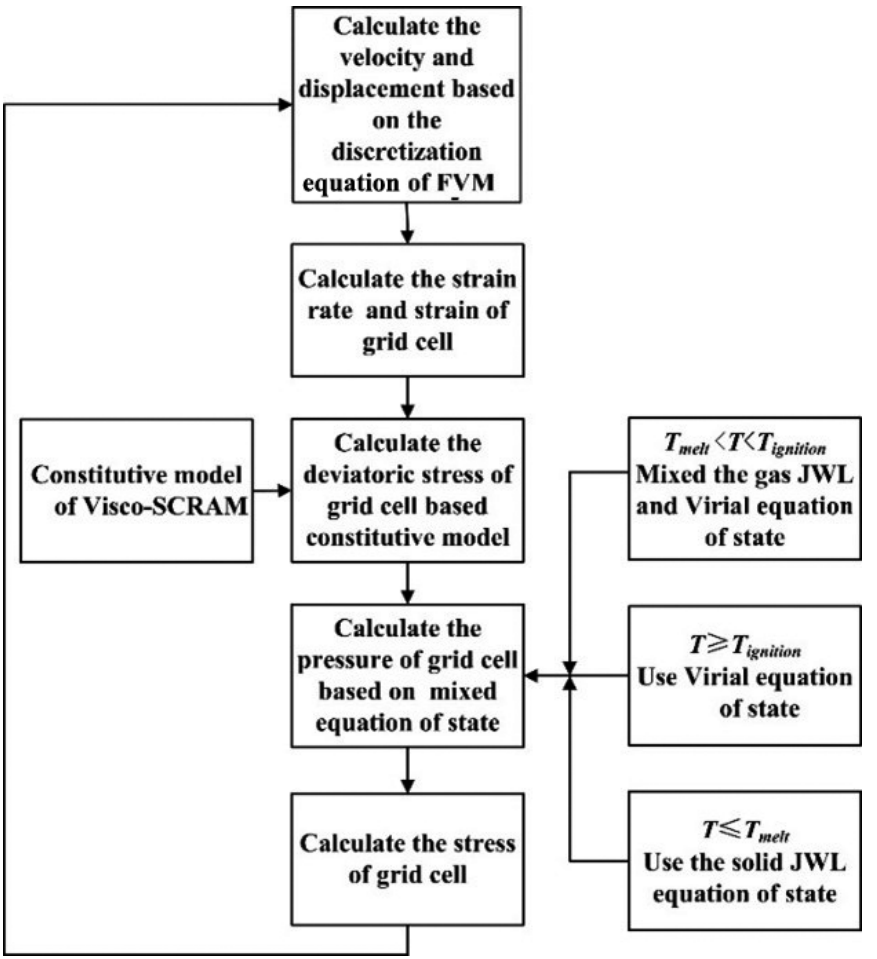

Figure 10. Flowchart for combustion reaction of explosive

7.2 Numerical example 1

The mixed combustion EOS is used to study combustion reaction of the explosive. All the simulations presented in this section are performed with a FORTRAN-based finite volume method. The explosive model is the same as the model introduced in the 5 section in this article, as shown in Figure 6. The PBX9501 explosive is used in this section, the relevant parameters of the PBX9501 explosive are provided in Tables 1 to 5. The pressure load shown in Equation 27 is applied at the far-right side of the model (bottom of the explosive, x = 400 mm).

In order to study the combustion reaction of the explosive, the initial temperature of the bottom of the explosive model is set to 600 K, whereas the other parts are set to 300 K. The mixing EOS is used to calculate the pressure of the combustion process. Due to the Arrhenius equation used in this study, the ignition threshold criterion is $dT/dt \rightarrow \infty$ pragmatically indicating a run0awa reaction [39]. When the explosive is ignited, the temperature increases indefinitely. However, the temperature after ignition is not calculated in this study; therefore, during the calculation, the temperature after ignition is set to 3000 K. The results are shown in Figures 11-13.

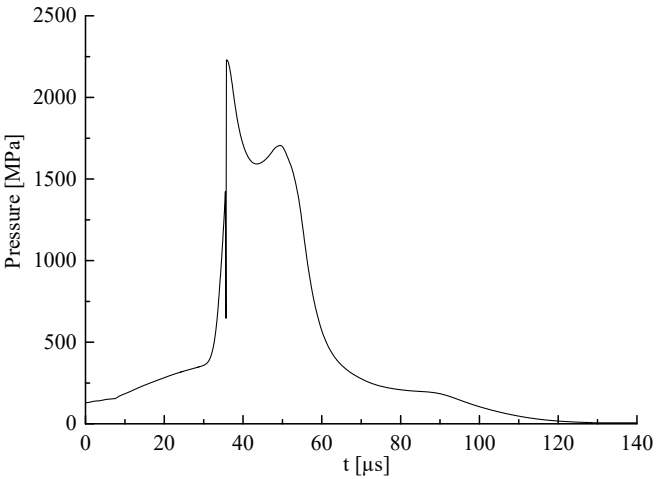

(a)

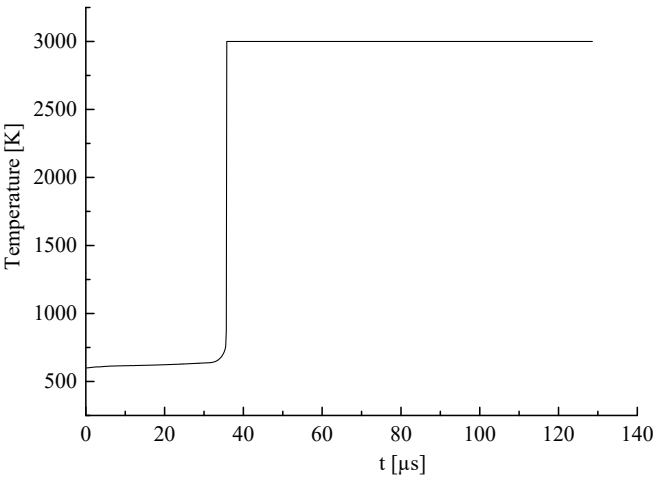

(b)

Figure 11. Pressure (a) and temperature (b) time-history curve at point A

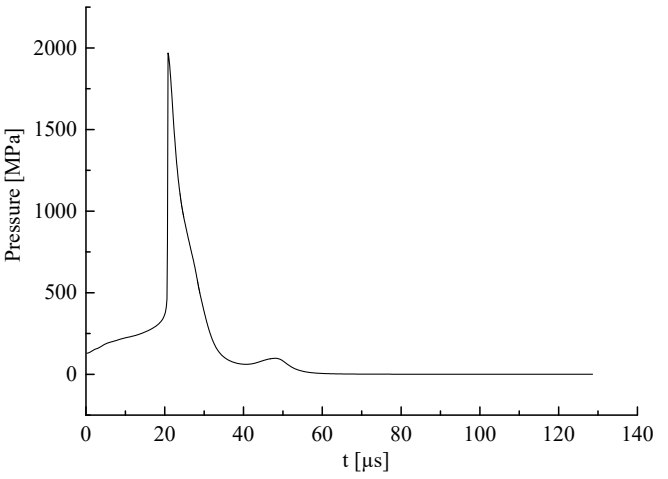

(a)

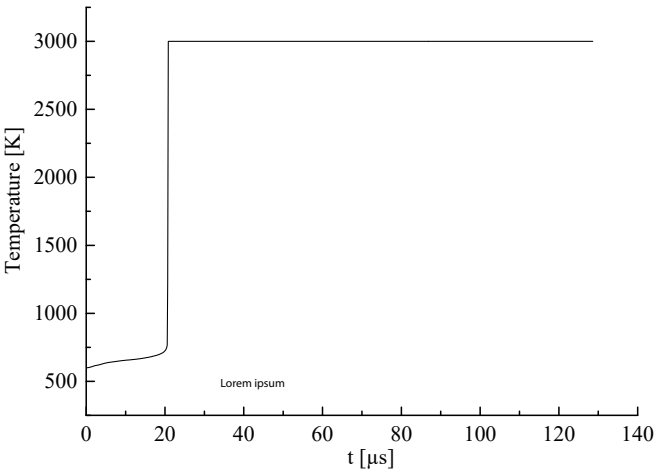

(b)

Figure 12. Pressure (a) and temperature (b) time-history curve at point B

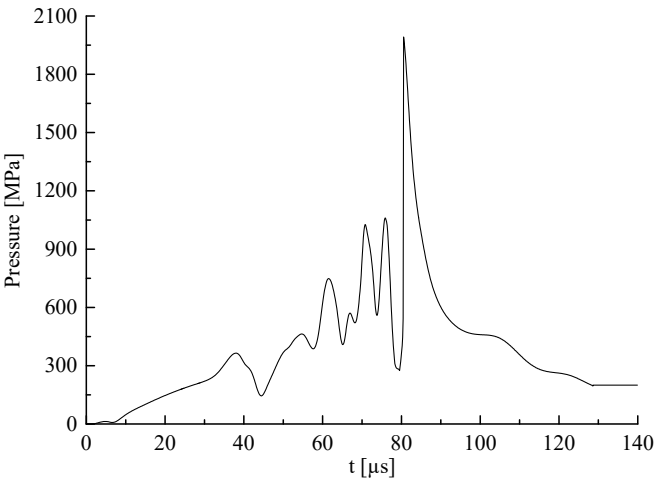

(a)

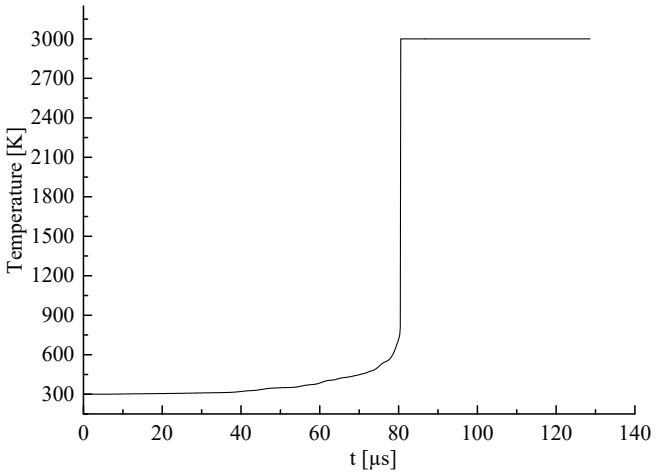

(b)

Figure 13. Pressure (a) and temperature (b) time-history curves at point C

In Figure 11, it can be seen that when the calculation time is approximately 40 μs, the peak pressure of the bottom of the explosive suddenly rises to 2.3 GPa, the temperature increases sharply, and then the pressure gradually decreases. This indicates that the explosive has a combustion reaction. The time of combustion reaction is consistent from the pressure and temperature time-history curves, and the pressure time-history curve and pressure peak conform to the law of the combustion reaction of the explosive.

In Figure 12, the point B is the grid cell at the upper corner of the bottom of the explosive. The temperature time-history curve shows that the temperature increases sharply when the calculated time is approximately 20 μs. The pressure time-history curve shows that the peak pressure is 2 GPa, and then the pressure gradually decreases. This indicates that the grid cell at point B has a combustion reaction. Moreover, it can be seen that the time of combustion reaction at the corner grid cell in Figure 12 is approximately 20 μs, while the time of combustion reaction at the bottom grid cell in Figure 11 is approximately 40 μs. Because that the grid cell in Figure 12 is located at the upper corner of the bottom of the explosive, a stress concentration occurs in this grid cell, so the grid cell in Figure 12 first has a combustion reaction.

In Figure 13, the temperature time-history curve shows that the temperature increases sharply when the calculated time is approximately 80 μs. The pressure time-history curve shows that the peak pressure of the grid cell at point *C* is 2 GPa, and then the pressure gradually decreases. This indicates that the grid

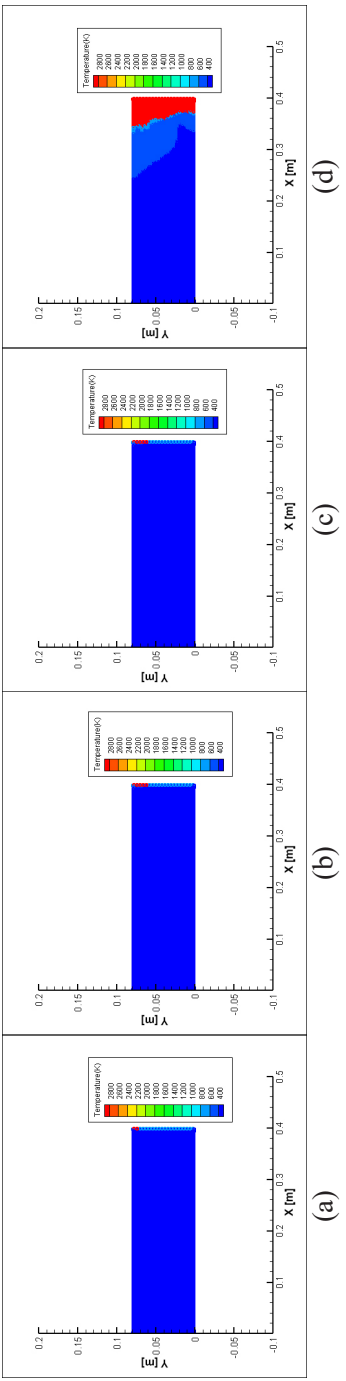

Figure 14. Temperature nephograms at *t*: 20 (a), 100 (b), 130 (c) and 140 µs (d)

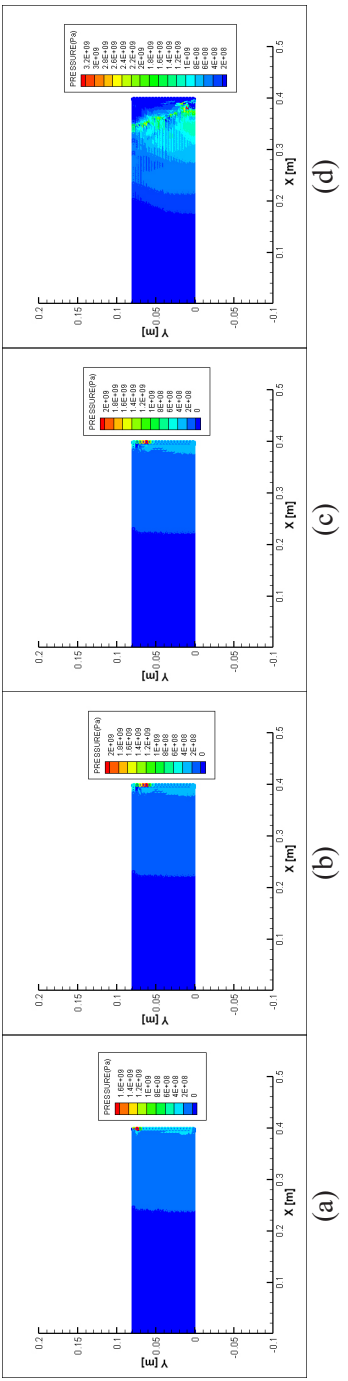

Figure 15. Pressure nephograms at *t*: 20 (a), 100 (b), 130 (c) and 140 µs (d)

cell at point C has a combustion reaction. From comparing Figures 12 and 13, it is observed that the time of combustion reaction at point B is 20 μs, while the time of combustion reaction at point C is 80 μs, it indicates that the pressure wave gradually propagates from the bottom of the explosive to the middle of the explosive. This, in turn, indicates that the propagation law conforms to the combustion reaction law of the explosives.

To further analyze the propagation law of combustion reaction, the temperature and pressure nephograms at different times are output, and the results are shown in Figures 14 and 15. In Figures 14 and 15, when the calculation time is 20 μs, it can be seen from the temperature nephograms that a "hot spot" area has clearly formed at the top corner of the bottom of the explosive (at point B), the "hot spot" area is the red area in Figure 14. The pressure nephograms show that the maximum value of the pressure occurs in the "hot spot" area, and maximum value of the pressure is 1.6 GPa; it indicates that the explosive undergoes a combustion reaction. As the grid cell at the top corner of the bottom of the explosive undergoes a stress concentration, the grid cell at the top corner of the bottom of the explosive first undergoes the combustion reaction. The results from the pressure and temperature nephograms are consistent with those from the time-history curve in Figure 12.

As the calculation time increases, when the calculation time is 140 μs, the temperature nephograms show that the "hot spot" area is expanding, the pressure nephograms show that the pressure wave has propagated to the middle of the explosive, the pressure peak is 3.2 GPa, it indicates that the combustion reaction propagates from the bottom of the explosive to the middle of the explosive. The results conform to the combustion reaction law of the explosive.

7.3 Numerical example 2

The explosive model is shown in Figure 16. The PBX9501 explosive is used in this example, the relevant parameters of the PBX9501 explosive are provided in Tables 1 to 5. The pressure load shown in Figure 17 is applied at the far-right side of the model (bottom of the explosive, x = 400 mm).

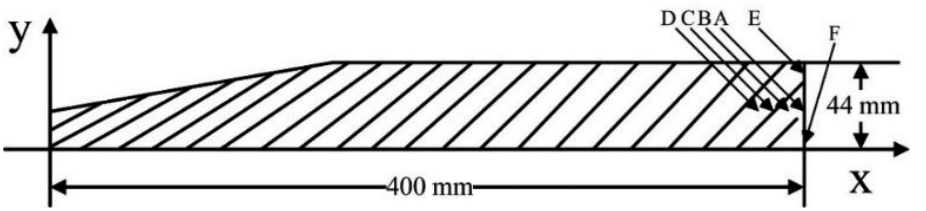

Figure 16. The model of explosive

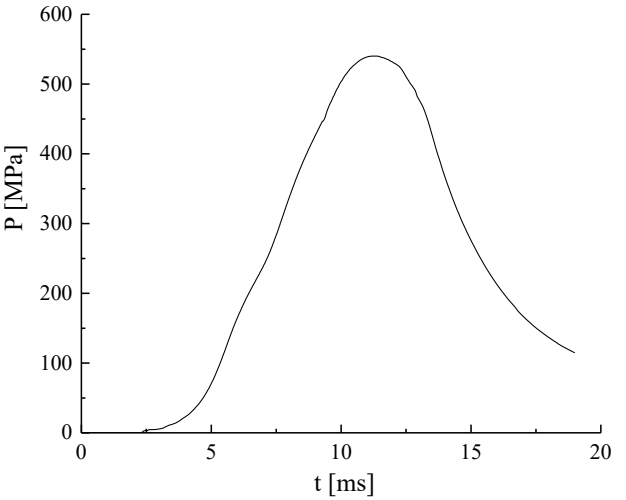

Figure 17. Loading history used

In order to study the combustion reaction of the explosive, the initial temperature of the bottom of the explosive model is set to 520 K, whereas the other parts are set to 300 K. The mixing EOS is used to calculate the pressure of the combustion process. Because the chemical kinetic Arrhenius equation is used in this study, the ignition temperature criterion is $dT/dt \rightarrow \infty$ [39]. When the explosive is ignited, the temperature increases indefinitely. However, the temperature after ignition is not calculated in this study; therefore, during the calculation, the temperature after ignition is set to 3000 K. The results are shown in Figures 18-20.

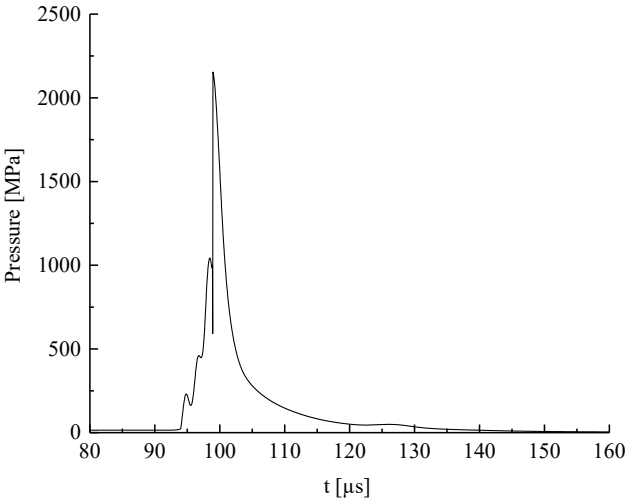

(a)

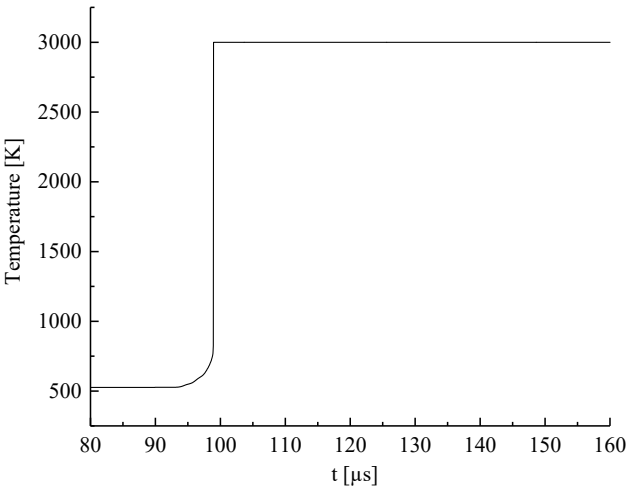

(b)

Figure 18. Pressure (a) and temperature (b) time-history curve at point A

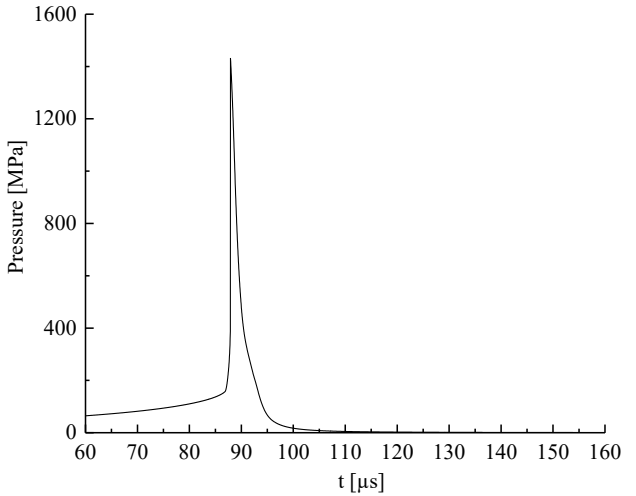

(a)

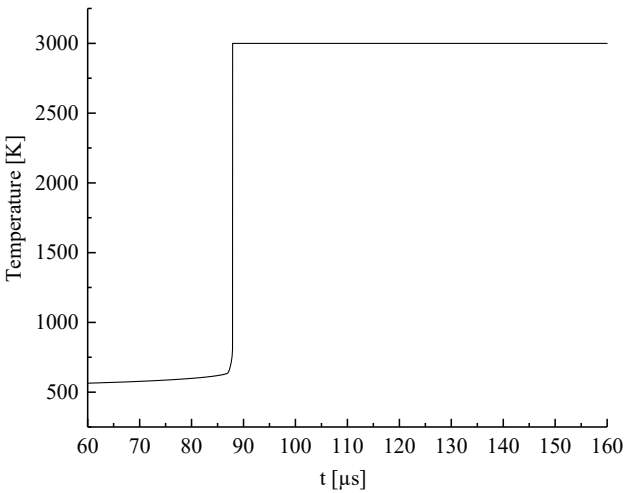

(b)

Figure 19. Pressure (a) and temperature (b) time-history curve at point E

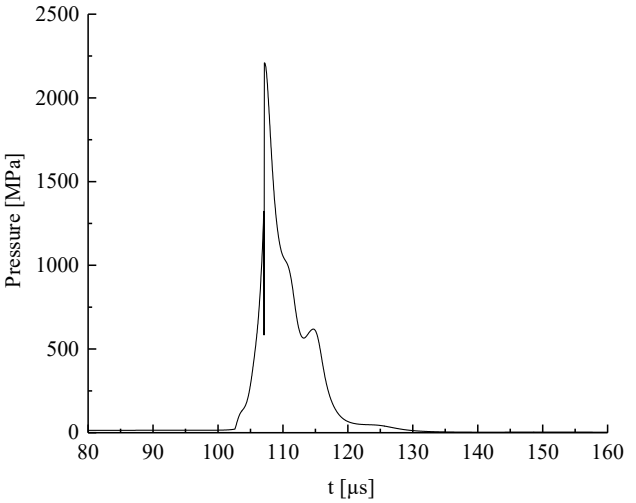

(a)

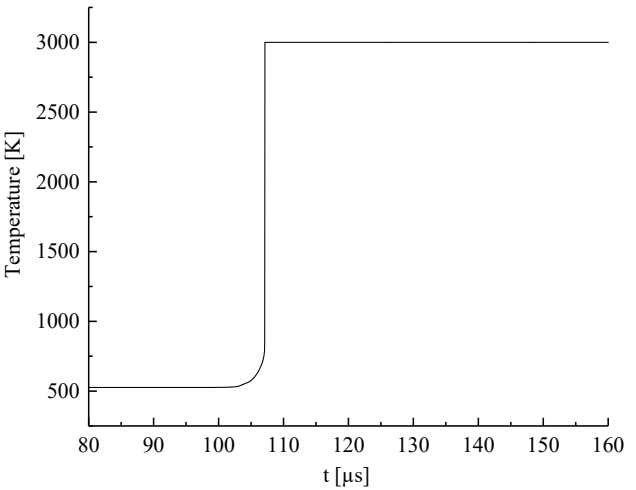

(b)

Figure 20. Pressure (a) and temperature (b) time-history curve at point F

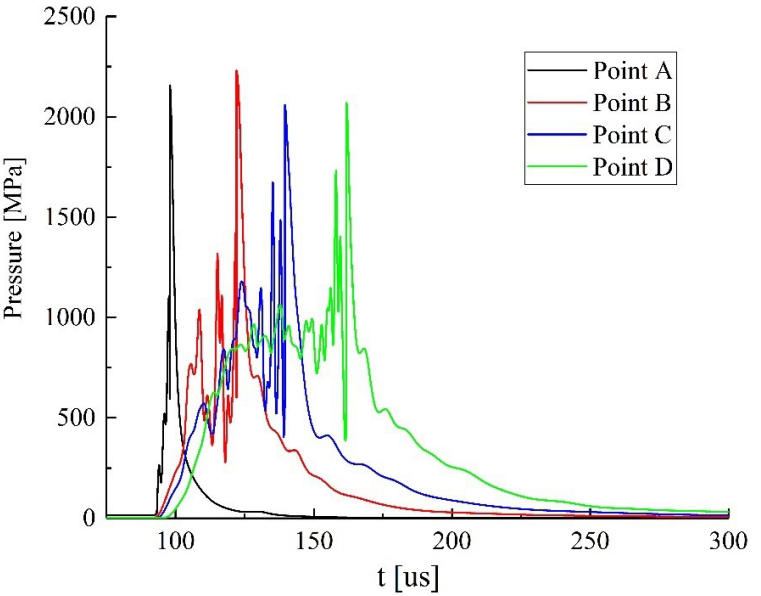

Figure 21. Pressure time-history curve at different points

In Figure 18, it can be seen that when the calculation time is approximately 100 μs, the peak pressure of the grid cell at point A suddenly rises to 2.2 GPa, then the pressure gradually decreases, the temperature increases sharply. In Figure 19, when the calculation time is approximately 90 μs, the peak pressure of the grid cell at point E suddenly rises to 1.4 GPa, then the pressure gradually decreases, the temperature increases sharply. In Figure 20, when the calculation time is approximately 110 μs, the peak pressure of the grid cell at point F suddenly rises to 2.2 GPa, and then the pressure gradually decreases, the temperature increases sharply. From Figures 18 to 20, the results indicate that the grid cell at points A, E, F undergoes a combustion reaction. The pressure and temperature time-history curves show that the combustion reaction time of the explosive is consistent, the trends of the pressure conform to the combustion reaction law of the explosive. Figure 21 shows the pressure time-history curve at different points A, B, C, D, the pressure peaks at different points are all above 2 GPa, it can be seen that the pressure wave is gradually propagating from the bottom of the explosive to the front of the explosive. It indicates that the combustion reaction propagates from the bottom of the explosive to the front of the explosive. The results conform to the combustion reaction law of the explosive. To further analyze the propagation law of combustion reaction, the temperature and pressure nephograms at different times are output, and the results are shown as Figures 22 and 23.

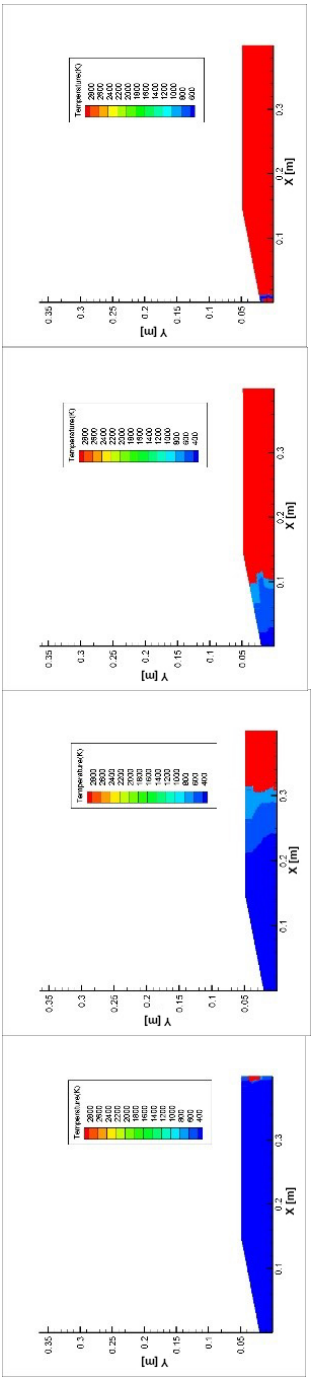

Figure 22. Temperature nephograms at *t*: 100 (a), 200 (b), 300 (c) and 380 µs (d)

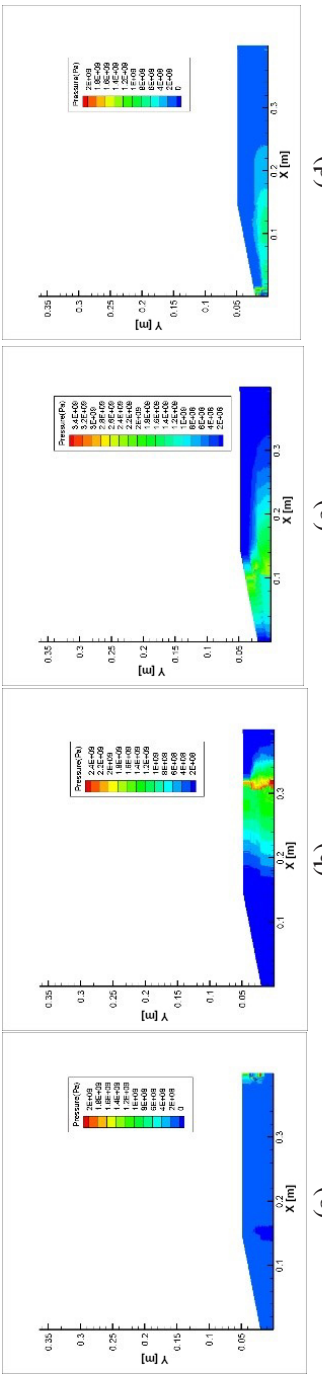

Figure 23. Pressure nephograms at *t*: 100 (a), 200 (b), 300 (c) and 380 µs (d)

In Figures 22 and 23, when the calculation time is 100 μs, it can be seen from the temperature nephograms that a "hot spot" area has clearly formed at the bottom of the explosive, the "hot spot" area is the red area in Figure 22. The pressure nephogram shows that the pressure peak at the "hot spot" area is 2.0 GPa, it indicates that the combustion reaction takes place.

As the calculation time increases, when the calculation time is 200 μs, the Figure 22(b) show that the "hot spot" area of temperature is expanding to the middle of the explosive, the Figure 23(b) show that the pressure wave is gradually propagating from the bottom of the explosive to the middle of the explosive. When the calculation time is 380 μs, the "hot spot" area of temperature is continuously spreading from the middle to the front of the explosive; the pressure wave is gradually propagating from the middle to the front of the explosive. The results are consistent with those from the time-history curve. It indicates that the results conform to the combustion reaction law of the explosive.

In the two examples, the temperature at the bottom of explosive model is 500 or 600 K, due to the high temperature at the bottom of the explosive, the bottom of explosive subjected the pressure load has a combustion reaction, and the combustion reaction propagates from the bottom of the explosive to the front of the explosive. However, when the temperature at the bottom of explosive model is 300 K, as shown in Figure 9, the explosive will not have a combustion reaction, the results indicate that when the bottom of the explosive is heated to a certain temperature, the bottom of the explosive subjected to pressure will have a combustion reaction.

8 Conclusions

- A computer program based on the FVM and Visco-SCRAM is developed for describing the combustion reaction of the explosive. First, the ignition temperature of explosive is studied. The variation trends of the temperature and stress of explosive subjected to a pressure load are calculated. The results show that the ignition temperature of PBX9501 explosive is between 750 and 800 K. The results are verified by comparing with that of extant studies. Second, the mixed combustion EOS is proposed to solve the combustion problem of explosives in this paper. The combustion reaction of the explosive subjected to the pressure load is studied. The results are consistent with the law of combustion reaction. In addition, it indicates that when the bottom of the explosive is heated to a certain temperature, the bottom of the explosive subjected to pressure will have a combustion reaction. This conclusion has

important value for studying the effect of base gap on the launch safety of explosive.

- The finite volume method is successfully applied to the field of mechanics of explosion in this paper, this study can be applied to structural protection engineering, blasting engineering and explosive safety engineering, it has important theoretical and application value. However, the detonation of the explosives after combustion is not discussed in the two examples, it will be the focus of future research.

Acknowledgements

This research was funded by National Natural Science Foundation of China [grant number 11902071]; "Academic backbone" Project of Northeast Agricultural University of China [grant number 54980412] and Postdoctoral Foundation of Heilongjiang Province of China [grant number LBH-Z19042].

References

[1] Liu, Y. *Experimental Study and Numerical Simulation on Mechanical Behavior of Polymer-Bonded Explosives.* PhD. thesis, Beijing Institute of Technology, Beijing, **2018**.

[2] Zhang, M.; Zhang, C.; Ruan, W. Impact Initiation Experiment and Numerical Simulation of Charge of Armor-piercing Explosive Projectile. *J. Ballist.* **2020**, *32*(3): 9-13.

[3] Guo, C.; Guo, S.; Qian, J. Numerical Simulation on Shock Critical Initiation Velocity of Cylindrical Covered Charge by Multiple Fragment Impacts. *Combust. Explos. Shock Waves* **2020**, *40*(6): paper 062301.

[4] Fan, Y.; Wang, J.; Xie, Q. Experimental and Numerical Simulation Study on the Shaped Charge Jet Impact of a Fuze. *J. Vibration Shock* **2020**, *39*(22): 261-267.

[5] Liu, R.; Han, Y.; Dai, X. Numerical Simulation on the Influence of the Initial Crack on Polymer Bonded Explosive Ignition Under Low Velocity Impact. (in Chinese) *Chin. J. Energ. Mater.* **2019**, *27*(10): 812-818.

[6] Ren, H.; Li, W.; Ning, J. Effect of Temperature on the Impact Ignition Behavior of the Aluminum/Polytetrafluoroethylene Reactive Material Under Multiple Pulse Loading. *Mater. Des.* **2020**, *189*: paper 108522; DOI: 10.1016/j.matdes.2020.108522.

[7] Ren, H.; Li. W.; Ning, J.; Liu, Y. The Influence of Initial Defects on Impact Ignition of Aluminum/Polytetrafluoroethylene Reactive Material. *Adv. Eng. Mater.* **2020**, *22*(3): paper 1900821; DOI: 10.1002/adem.201900821.

[8] Hanina, E.; Partom, Y.; Havazelet, D.; Sadot, O. Prediction of Low-velocity-Impact Ignition Threshold of Energetic Materials by Shear-band Mesoscale Simulations.

J. Energ. Mater. **2018**, *36*(3): 325-338; DOI: 10.1080/07370652.2017.1421726.
[9] Dai, X.; Wen, Y.; Wen, M.; Huang, F.; Li, M.; Deng, C. Projectile Impact Ignition and Reaction Violent Mechanism for HMX-Based Polymer Bonded Explosives at High Temperature. *Propellants Explos. Pyrotech.* **2017**, *42*(7): 799-808; DOI: 10.1002/prep.201600130.
[10] Li, S.; Duan, Z.; Zhang, Z.; Ou, Z.; Huang, F. Numerical Simulation on Shock Initiation of Aluminized Melt-Cast Explosives. (in Chinese) *Acta Armamentarii* **2020**, *41*(S2): 211-217.
[11] Dienes, J.K.; Kershner, J.D. Multiple-Shock Initiation via Statistical Crack Mechanics. *Proc. 11th Int. Detonation Symp.,* Snowmass, US, **1998**, 717-724.
[12] Dienes, J.K.; Zuo, Q.H.; Kershner, J.D. Impact Initiation of Explosives and Propellants via Statistical Crack Mechanics. *J. Mech. Phys. Solids* **2006**, *54*(6): 1237-1275; DOI: 10.1016/j.jmps.2005.12.001.
[13] Addessio, F.L.; Johnson, J.N. A Constitutive Model for the Dynamic Response of Brittle Materials. *J. Appl. Phys.* **1990**, *67*(7): 3275-3286; DOI: 10.1063/1.346090.
[14] Bonnett, D.L.; Butler, P.B. Hot-Spot Ignition of Condensed Phase Energetic Materials. *J. Propul. Power* **1996**, *12*(4): 680-690; DOI: 10.2514/3.24089.
[15] Bai, Z.-L.; Duan, Z.-P.; Wen, L.-J.; Zhang, Z.-Y.; Ou, Z.-C.; Huang, F.-L. A Modified Mesoscopic Reaction Rate Model for Shock Initiation of PBX. (in Chinese) *Chin. J. Energ. Mater.* **2019**, *27*(8): 629-635; DOI: 10.11943/CJEM2018354.
[16] Huang, K. *Numerical Study on Shock Initiation and Detonation of PBX Explosive.* PhD thesis, Institute of Applied Physics and Computational Mathematics, Beijing, **2020**.
[17] Zhang, Y.-G.; Lou, J.-F.; Zhou, T.-T.; Hong, T.; Zhang, S.-D. Initial Study on Constitutive Model of PBXs via Viscoelastic Statistical Crack Mechanics Including Anisotropic Damage. (in Chinese) *Chin. J. High Pressure Phys.* **2016**, *30*(4): 301-310; DOI: 10.11858/gywlxb.2016.04.006.
[18] Yang, K.; Wu, Y.-Q.; Jin, P.-G.; Huang, F. Damage-Ignition Simulation for Typical Pressed and Casted PBX under Crack-extruded Loading. (in Chinese) *Chin. J. Energ. Mater.* **2020**, *28*(10): 975-983; DOI: 10.11943/CJEM2020170.
[19] Tang, M.-F.; Gan, H.-X.; Wen, M.-P.; Wang, S.-N. Simulation and Experimental Study on the Thermal Shock Behavior of Notched PBX Cylinders. (in Chinese) *Chin. J. Energ. Mater.* **2021**, *29*(1): 41-47; DOI: 10.11943/CJEM2019237.
[20] Zhang, Q.-L.; Duan, Z.-P.; Meng, F.-X.; Nan, H.; Wang, X.-J.; Huang, F.-L. Experiments and Numerical Simulations of Penetration Stability of Cast Charge PBX-1. (in Chinese) *Chin. J. Energ. Mater.* **2021**, *29*(2): 107-113; DOI: 10.11943/CJEM2020203.
[21] Li, X. *Investigations on Damage and Initiation Mechanism of PBX Charge During Penetration.* PhD thesis, Harbin Institute of Technology, Harbin, **2020**.
[22] Zhang, Z.; Wu, Y.-Q. Effect of Sugar Particles on Non-Shock Ignition of Two Kinds of Single Compounds HMX and RDX. (in Chinese) *Chin. J. Energ. Mater.* **2019**, *27*(10): 805-811; DOI: 10.11943/CJEM2018360.
[23] Qin, J. *Experimental Investigation and Numerical Modelling of non-Shock Ignition*

Mechanism in PBX Explosives. PhD thesis, Graduate School of National University of Defense Technology, Changsha, **2014**.

[24] Dienes, J.K.; Middleditch, J.; Kershner, J.D.; Zuo, O.; Starobin, A. Progress in Statistical Crack Mechanics: An Approach to Initiation. *Proc. 12th Symp. Int. on Detonation*, Annapolis, US, **2002**, 793-799.

[25] Sun, H. *Study on Temperature Fluctuation and Damage Evolution of Polymer Bonded Explosive under Emission and Penetration Conditions.* MSc. dissertation, Nanjing University of Science and Technology, Nanjing, **2018**.

[26] Zhang, Y.; Lou, J.; Hong, T. Modification of Visco Statistical Crack Mechanics for PBX. (in Chinese) *Chin. J. High Pressure Phys.* **2015**, *29*(1): 9-14.

[27] Yang, S.; Liu, F.; Feng, L.; Turner, I. A Novel Finite Volume Method for the Nonlinear Two-Sided Space Distributed-Order Diffusion Equation with Variable Coefficients. *J. Comput. Appl. Mathematics* **2021**, *388*: paper 113337; DOI: 10.1016/j.cam.2020.113337.

[28] Liu, H.; Zheng, X.; Fu, H.; Wang, H. Analysis and Efficient Implementation of Alternating Direction Implicit Finite Volume Method for Riesz Space-Fractional Diffusion Equations in Two Space Dimensions. *Numer. Methods Partial Differential Eq.* **2020**, *37*(1): 818-835; DOI: 10.1002/num.22554.

[29] Mohammadi, M.; Vakilipour, S.; Ormiston, S. Newton Linearization of the Navier-Stokes Equations for Flow Computations Using a Fully Coupled Finite Volume Method. *Appl. Mathematics Comput.* **2021**, *397*: paper 125916; DOI: 10.1016/j.amc.2020.125916.

[30] Berberich, J.P.; Chandrashekar, P.; Klingenberg, C. High Order well-balanced Finite Volume Methods for multi-Dimensional Systems of Hyperbolic Balance Laws. *Comput. Fluids* **2021**, *219*: paper 104858: DOI: 10.1016/j.compfluid.2021.104858.

[31] Fatahillah, A.; Setiawan, T.B.; Sholihin, A. Numerical Analysis of Ice Freezing Processes of Block Ice Production in a Brine Tank Factory Using the Finite Volume Method. *J. Phys.: Conf. Ser.* **2021**, *1832*: paper 012023; DOI: 10.1088/1742-6596/1832/1/012023.

[32] Zhang, S.; Khoo, B.C.; Zhang, A.M. Study of Three-Dimensional Air Gun Bubble Pulsation and the Surrounding Fluid Pressure with Finite Volume Method. *Ocean Eng.* **2021**, *221*(1): paper 108500; DOI: 10.1016/j.oceaneng.2020.108500.

[33] Liu, B.; Lu, W. Surrogate Models in Machine Learning for Computational Stochastic multi-Scale Modelling in Composite Materials Design. *Int. J. Hydromechatronics* **2022**, *5*(4): 336-365; DOI: 10.1504/ijhm.2022.127037.

[34] Liu, B.; Nam, V.-B.; Zhuang, X.; Fu, X.; Rabczuk, T. Stochastic full-Range Multiscale Modeling of Thermal Conductivity of Polymeric Carbon Nanotubes Composites: A Machine Learning Approach. *Compos. Struct.* **2022**, *289*(1): paper 115393; DOI: 10.1016/j.compstruct.2022.115393.

[35] Yu, Y. *Study on Finite Volume Method for Dynamic Response of Thin Plate Structure.* M.Sc. dissertation, Harbin Engineering University, Harbin, **2011**.

[36] Dienes, J.K.; Kershner, J.D. Crack Dynamics and Explosive Burn via Generalized Coordinates. *J. Comput.-Aided Mater. Des.* **2000**, *7*(3): 217-237; DOI:

10.1023/A:1011874909560.
[37] Zhao, S. A *Viscoelastic Statistic Crack Constitutive Model for Mechanical Response and the non-Shock Ignition of High Explosives.* M.Sc. dissertation, National University of Defense Technology, Harbin, **2011**.
[38] Bennett, J.G.; Haberman, K.S.; Johnson, J.N.; Asay, B.W. A Constitutive Model for the non-Shock Ignition and Mechanical Response of High Explosives. *J. Mech. Phys. Solids* **1998**, *46*(12): 2303-2322; DOI: 10.1016/S0022-5096(98)00011-8.
[39] Sun, B.; Duan, Z.; Wan, J. Investigation on Ignition of an Explosive Charge in a Projectile During Penetration Based on Visco-SCRAM Model. *Explos. Shock Waves* **2015**, *35*(5): 689-695.
[40] Volk, F.; Bathelt, H. Application of the Virial Equation of State in Calculating Interior Ballistics Quantities. *Propellants Explos.* **1976**, *1*(1): 7-14; DOI: 10.1002/prep.19760010104.

Received: April 13, 2022
Revised: June 28, 2023
First published online: June 30, 2023